# Generator-level acceptance for the measurement of the inclusive cross section of W-boson and Z-boson production in pp collisions at $\sqrt{s} = 5\,\mathrm{TeV}$ with the CMS detector at the LHC

by

Alexander Andriatis

Submitted to the Department of Physics
in partial fulfillment of the requirements for the degree of

Bachelor of Science in Physics

at the

MASSACHUSETTS INSTITUTE OF TECHNOLOGY

February 2018



Author .......... Signature redacted ................
Department of Physics
January 19, 2018

Certified by.. Signature redacted .....................
Markus Klute
Associate Professor of Physics
Thesis Supervisor

Accepted by . Signature redacted .....................
Scott Hughes
Interim Physics Associate Head

# Generator-level acceptance for the measurement of the inclusive cross section of W-boson and Z-boson production in pp collisions at $\sqrt{s} = 5\,\text{TeV}$ with the CMS detector at the LHC

by

Alexander Andriatis

Submitted to the Department of Physics
on January 19, 2018, in partial fulfillment of the
requirements for the degree of
Bachelor of Science in Physics

## Abstract

The inclusive cross section of vector boson production in proton-proton collisions is one of the key measurements for constraining the Standard Model and an important part of the physics program at the LHC. Measurement of the inclusive cross section requires calculating the detector acceptance of decay products. The acceptance of the CMS detector of leptonic decays of W and Z bosons produced in pp colisions at $\sqrt{s} = 5\,\text{TeV}$ is calculated using Monte Carlo event simulation. Statistical and systematic uncertainties on the acceptance measurement from PDF and $\alpha_s$ uncertainty and higher-order correction are reported. The use of the calculated acceptance in combination with measurements of detector efficiency, luminosity, and particle counting to determine the inclusive cross section is outlined. A total integrated luminosity of $331.64\,\text{pb}^{-1}$ from 2015 and 2017 CMS data at $\sqrt{s} = 5\,\text{TeV}$ is available for the calculation of the inclusive cross section.

Thesis Supervisor: Markus Klute
Title: Associate Professor of Physics

# Acknowledgments

The author greatfully acknowledges the guidance and support of Prof. Markus Klute in this research and throughout the undergraduate education. The author also greatly thanks postdoctoral fellows Dr. Aram Apyan, Dr. Mariarosaria D'Alfonso, and Dr. Andrea Carlo Marini as well as graduate students Stephanie Brandt and Xinmei Niu for their expertise and guidance. The author is very grateful for the many opportunities to travel to and work at CERN, supported by the UROP and the MISTI-France programs.

# Contents

# List of Figures

# List of Tables

# Chapter 1

# Introduction

The Large Hadron Collider (LHC) is a proton-proton collider housed in a 27 km circumference tunnel located at CERN in Geneva, Switzerland. The LHC performs head-on collisions of two proton beams at a nominal energy of 7 TeV and a design luminosity of $10^{34}\,\mathrm{cm}^{-2}\,\mathrm{s}^{-1}$ [2]. The LHC is also capable of performing lead-lead and lead-proton collisions. The purpose of the LHC is to study electroweak symmetry breaking and the Higgs mechanism. The observation of the Higgs boson in 2012 completed the Standard Model of particle physics. Other areas of investigation at the LHC include Beyond Standard Model new physics at higher energy scales, such as supersymmetry, and the search for extra dimmensions and dark matter. In addition, the capacity to perform heavy-ion collisions allows for the exploration of quark-gluon plasma, a high temperature, high density state of matter that recreates conditions in the early universe.

The LHC is uniquely suited to explore physcis at the TeV scale due to its improvement in energy and luminosity over previous hadron colliders. The Tevatron at Fermilab, the previous record-holder, performed proton-antiproton ($p\bar{p}$) collisions with beam energy of 0.98 TeV and peak luminosity of $4 \times 10^{32}\,\mathrm{cm}^{-2}\,\mathrm{s}^{-1}$ [3]. For proton-proton collisions at a design center of mass energy of $\sqrt{s} = 14\,\mathrm{TeV}$ the total collision cross section is expected to be $\sim 10^{-25}\,\mathrm{cm}^2$ of which inelastic scattering is $\sim 8.5 \times 10^{-26}\,\mathrm{cm}^2$ [4]. For a design luminosity of $10^{34}\,\mathrm{cm}^{-2}\,\mathrm{s}^{-1}$ this yields a collision rate of 850 million events per second. With a design of 2808 proton bunches per beam at 25 ns spacing and beam revolution rate of 11245 per second, there are 31.6 million bunch crossings per second at each interaction point, with an average of 27 inelastic scattering events per crossing.

In an inelastic proton-proton scattering the constituent quarks and gluons interact to create a wide spectrum of new particles that propagate outwards from the interaction point. The high energy of the incoming particles allows the creation of highly massive particles that are never otherwise produced in nature. Heavy particles are highly unstable and quickly decay — it is the purpose of particle detectors to observe the decay products and their kinematics in order to understand the physics of the particles and ineractions involved in the collisions. At the LHC proton beams cross at four interaction points, around which are located seven total detectors. Two general-purpose detectors, the Compact Muon Solenoid (CMS) and A Toroidal LHC ApparatuS (ATLAS) are sensitive to the broadest possible range of signals, while the others are designed for specialized research [5, 6].

In proton-proton collisions, W and Z bosons are produced through hard scattering of colliding partons. The leading order production process is the Drell-Yan quark-antiqurark anhilation $q\bar{q} \to V$, where V is a vector boson, the Feynman diagrams of which are depicted in figure 1-1. Drell-Yan vector boson production and leptonic decay is one of the best-understood processes at the LHC, serving as well-known backgrounds in other Standard Model (SM) and Beyond Standard Model (BSM) searches, used as fundamental tools for detector calibration and performance studies, and useful for luminosity measurements. The total production is given by $N = \sigma_{inc} \times \mathcal{L}$ where $\sigma_{inc}$ is the inclusive cross-section of a given process and $\mathcal{L}$ is the integrated luminosity. Measurement of the inclusive cross-section of W and Z boson production in proton-proton collisions is an important test for the Standard Model of particle physics.

The Standard Model is a theory of elementary particles and fundamental forces that has sucessfully explained almost all experimental observations and predicted new phonomena in particle physics. The theory contains seventeen different particles, which are either fermions, particles with half-integer spin that are the constituents

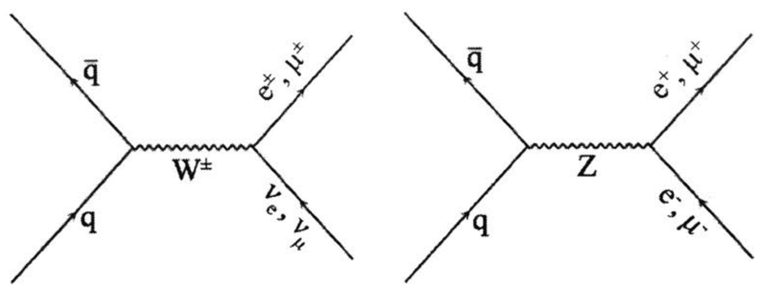


Figure 1-1: Feynman diagrams of Drell-Yan $W^{\pm}$ and $Z^0$ production with leptonic decay. Source: Dilsiz, K. and Tiras, E., 2017 [1].

of matter, or bosons, with integer spin that are mediators of interactions. Fermions derive their name from following Fermi-Dirac statistics, which describes the distribution of identical particles over energy states in which no two particles can occupy the same energy state, also known as the Pauli Exclusion principle. Becasue two identical fermions cannot have the same quantum numbers, they uphold intuition about ordinary matter that cannot occupy the same space at the same time. Bosons on the other hand get their name from Bose-Einstein statistics, which describes the distribution of identical particles not limited by single occupancy of states.

The elementary fermions of the standard model all have spin $\frac{1}{2}$ and are grouped according to the charges they carry. Quarks have mass, electric charge, color charge, and come in six flavors. Up-type quarks have an electric charge of $+\frac{2}{3}e$ and the three generations in order of increasing mass are up (u), charm (c), and top (t) quarks. The down-type quarks down (d), strange (s), and bottom (b) have electric charge of $-\frac{1}{3}e$. Every quark has a corresponding antiquark, with opposite electric and color charges.

The color charges are labeled as red, green, and blue, with corresponding antiquark colors antired, antigreen, and antiblue. Color is an SU(3) gauge symmetry and the defining feature of Quantum Chromodynamics (QCD), the theory describing the action of the strong force. Quarks are subject to the QCD phenomenon of color confinement, which states that color charged particles cannot be isolated, but must form color-neutral composite particles called hadrons. The principle of color confinement can be qualitatively described through the effects of quark separation. When a pair of color charges are separated, the gluon field between them, expressing the behavior of the strong force, acts in such a way that the creation of a new quark-antiquark pair is energetically favorable. Within hadrons, this repetitive process of virtual quark-antiquark pair production and annihilation forms a flux of particles known as the sea quarks. In particle decays, color confinement results in the formation of hadronic jets, which will be further discussed in the context of event simulaiton in section 3.

There are two families of hadrons - baryons and mesons. Baryons are made of three valence quarks, along with an accompanying sea of virtual quarks and gluons, and are therefore also fermions since they have a total half-integer value spin. Sea quarks The most familiar baryons are protons, containing two up quarks and one down quark, and neutrons, made of one up quark and two down quarks. Mesons have a valence quark and antiquark, and are therefore bosonic. The virtual quarks and gluons are important to keep in mind when considering the physics of proton-proton collisions, since it is often quarks from this sea that make up the hard scattering process of interest, and the rest of the particles form what is known as the underlying event, a chaotic process of interacting particles forming a hadronic background to the signal. Each constituent particle of the colliding hadron carries only a portion of the momentum involved in the collision, modeled through Parton Distribution Functions (PDFs), which will be discussed in greater detail in section 3 in the context of event generation and section 5 in the context of theoretical uncertainties on acceptance values.

The electric charge of quarks allows them to interact through the electromagnetic force as well, and also gives this property to charged composite particles, such as the proton and pion ($\pi^+$). Quarks allows interact through the weak nucelar force, which mediates interacton between particle flavors. Finally, the quarks are massive and therefore interact through gravity, making them the only fundamental particles that interact with all four fundamental forces.

The other type of fermions in the standard model are the leptons, which do not carry color charge. The three generations of leptons are electronic, muonic, and tauonic, with the electron ($e^-$), muon ($\mu^-$), and tau ($\tau^-$) having a charge of $-1e$

while their respective neutrino flavors $\nu_e$, $\nu_\mu$, and $\nu_\tau$ are neutral and have a much smaller, but sill non-zero mass. Although the Standard Model first assumed massless neutrinos, the observed phenomenon of neutrino oscillation, which occurs from the mixing of neutrino flavor and mass eigenstates, requires neutrinos with mass. The origin of the mass of the neutrino is one of the open questions of the Standard Model. The non-interaction of neutrinos with either the strong or electromagnetic forces along with their small mass makes them extremely difficult to detect. Each lepton has a corresponding antiparticle with an opposite charge, and in the theory of Majorana neutrinos it is proposed that the neutrio is its own antiparticle [7].

Elementary bosons of the standard model are the spin 1 gauge bosons, the force carriers mediating the strong, weak, and electromagnetic interactions and the spin 0 scalar Higgs boson (h), which generates the mass of elementary particles. Gluons, mediating the strong interaction between color charged particles, are massless, but the eight non-singlet gluon color states in SU(3) result in net color charge of gluons, leading to self-interaction. The electromagnetic force is mediated by photons ($\gamma$), which are massless, uncharged, and long-ranged. The theory of Quantum Electrodynamics (QED), a reletavistic quantum field theory of electromagnetism, describes the interaction of charged particles through the exchange of photons. The weak interaction between different flavors of quarks and leptons is mediated through the $W^{\pm}$ and $Z^0$ vector bosons. The theory of weak interaction is best described through electroweak theory, the unification of electromagnetism and weak interaction.

In the 1960's Glashow, Salam, and Weinberg proposed a theory of electroweak unification that was consistent with charged current interactions through the exchange of $W^{\pm}$ and predicted neutral current interactions through exchanges of $\gamma$ and $Z^0$. The neutral current is so named becasue an exchange of a $Z^0$ boson transfers energy or momentum without changing a particle's quantum numbers, so that charge and flavor remains the same. In 1973 the first obeservation of neutral current interaction was observed at CERN in the Gargamelle bubble chamber, designed to detect neutrinos [8, 9]. Two types of events were observed, one in which the neutrino interacts with an electron, and another in which the neutrino is scattered from a hadron.

The observation of neutral current was a strong support for electroweak theory, and called for the direct observation of $W^{\pm}$ and $Z^0$ bosons as a test of electroweak theory. The theory predicted their approximate masses on the order of 100 GeV and their coupling to leptons and quarks. To make a collider capable of producing particles in that range, the Super Proton Synchroton (SPS) at CERN was modified into a proton-antiproton collider (Sp$\bar{\text{p}}$S) capable of a beam energy of 315 GeV. The decay modes of $W^+$ are either to lepton-neutrino pairs $W^+ \rightarrow e^+\nu_e, \mu^+\nu_\mu, \tau^+\tau_e$ or to an up-type, down-type quark-antiquark pair $W^+ \rightarrow u\bar{d}, u\bar{s}, u\bar{b}, c\bar{d}, c\bar{s}, c\bar{b}$. The corresponding charge conjugates describe decays of $W^-$. Decays to a top quark are forbidden becasue it is more massive than the W. The $Z^0$ boson decays to leptons, neutrinos, or quarks and their corresponding antiparticles $Z^0 \rightarrow l^+l^-, q\bar{q}$. In a proton-antiproton collider the decay modes most useful for detection are the leptonic ones, since most of the high transverse momentum ($p_T$) background is from hadronic scattering, called the QCD background.

The Sp$\bar{\text{p}}$S and the Underground Area detectors UA1 and UA2 were designed to optimise detection of the leptonic decay modes. UA1 was a general purpose detector featuring the largest drift chamber of its time, a six-chambered cylinder 5.8 meters long and 2.3 meters in diameter [10]. An 0.7 Tesla magnetic field curved charged particles and allowed recording of their momentum, charge, and rate of energy loss. The chambers contained an argon-ethane gas mixture which was ionized by the passage of charged particles, releasing electrons, which drifted along an electric field made by 17,000 field wires and recorded by 6,125 sense wires. The geometric arrangement of the electric wires allowed for a three-dimensional reconstruction of collision events. The detector also featured electromagnetic and hadronic calorimeters and muon chambers [10]. One of the detector's big advantages was its excellent hermeticity, which allowed for accurate measurementsd of missing transverse energy ($E_T$) from escaping neutrinos. Its design informed later all-purpose detectors such as CMS. UA2 was built as a more specialized detector, focusing on high-granularity electromagnetic and hardronic calorimeters [11]. The discoveries of W and Z bosons by UA1 and UA2 were both announced in 1983 [12, 13, 14]. Carlo Rubbia, who proposed the conversion of SpS to a proton-antiproton coillider and was spokesperson for UA1, and Simon van der Meer, inventor of stochastic cooling of particle beams that allowed for the construction of the Antiproton Accumulator as an antiproton source for the experiment, shared the 1984 Nobel Prize in Physics for contributions to the discovery of W and Z bosons [15].

Precision studies of W and Z bosons were performed in the Large Electron-Positron Collider (LEP) at CERN from 1989 to 2000 [16, 17, 18]. Its construction created the 27 km tunnel now used by the LHC. A major factor in determining the size of the collider was the problem of synchrotron radiation, which scales to the fourth power in particle energy and is inversely proportional to the square of the dipole bending radius. Four detector complexes, ALEPH, DELPHI, L3, and OPAL were built around the four interaction points. The detectors all featured $4\pi$ hermiticity, silicon-based vertex detectors, electromagnetic and hadronic calorimeters of various resolution, and muon chambers. Differences across detector design led to redundancy in analysis and cancelation of systematic uncertainties in combined analyses [18]. The old SPS accelerator complex was used as a pre-accelerator for LEP, consisting of the old Proton Synchrotoron (PS) upgraded to a 3.5 GeV lepton synchrotron with additional linear accelerators and an Electron-Positron Accumulator, and SPS was upgraded to accelerate to 20 GeV. In the first phase of operation, LEP had 5,176 magnets and 128 accelerating cavities, giving a beam energy of 45.6 GeV for $Z^0$ production $e^+e^- \rightarrow Z^0$. LEP was upgraded in 1995 to run at higher energy for W pair production $e^+e^- \rightarrow W^+W^-$, using up to 288 accelerating cavities. The maximum beam energy achcieved was 209 GeV in 2000 before being shut down to be replaced by the LHC. Over its operation life about 4 million $Z^0$ bosons and 10,000 $W^{\pm}$ pairs were observed by each of the four detectors. The mass of and width of the Z were determined to be $M_z = 91.1874 \pm 0.0021$ GeV and $\Gamma_Z = 2.4952 \pm 0.0023$ GeV. The mass and width of the W were determined to be $M_W = 80.376 \pm 0.033$ GeV and $\Gamma_W = 2.195 \pm 0.083$ GeV [18]. Other precision measurments included the strong coupling constant, the leptonic effective electroweak mixing angle, the leptonic $\rho$ parameter, prediction of the top quark mass, and a 95% confidence level lower limit on the Higgs mass of 114.4 GeV, which contributed to Higgs searches at the LHC [18].

Measaurement of electroweak W and Z properties remain an important component of the physics program at the LHC. Higher energies allow the study of electroweak properties that are energy-dependent, such as the production cross section and the theory of perturbative QCD, as well as improvements in electroweak precision measurements such as the masses and widths of the W and Z bosons.

The total cross section is measured by computing

$$\sigma_{tot} \times B = \frac{N}{A \times \epsilon \times \mathcal{L}}$$

where $\sigma_{tot}$ is the inclusive cross section, $B$ is the branching ratio of a particular decay channel, $N$ is the number of signal events extracted from the data corresponding to the particular decay channel, $A$ is the detector acceptance of the fiducial phase space, $\epsilon$ is detector efficiency, and $\mathcal{L}$ is the total integrated luminosity.

This paper calculates the fiducial and kinematic acceptance of leptonic W and Z boson decays from proton-proton collisions at the LHC in the CMS detector at a center of mass energy of $\sqrt{s} = 5\,\text{TeV}$. The generator-level acceptance for leptonic decays of W and Z bosons is found using Monte Carlo simulation, and systematic uncertainties are calculated. The acceptance can be combined with measurements of efficiency, luminosity, particle count, and branching ratio to give the inclusive cross section. Calculation of the acceptance at $\sqrt{s} = 5\,\text{TeV}$ will contribute directly to the measurement of the inclusive cross section of W and Z bosons from proton-proton collision data during LHC reference runs in 2015 and 2017 with total integrated luminosities of $\mathcal{L} = 28.08\,\text{pb}^{-1}$ and $\mathcal{L} = 303.56\,\text{pb}^{-1}$ respectively [19]. The measurement of the cross section is a valuable validation of the standard model and is useful in further constraining Parton Distribution Functions that are used to make theoretical predictions about the standard model.

Measurements of inclusive W and Z boson production cross sections from proton-proton collisions have been previously measured by the CMS and ATLAS Collaborations at $\sqrt{s} = 7\,\text{TeV}$ [20, 21], $\sqrt{s} = 8\,\text{TeV}$ [22], and $\sqrt{s} = 13\,\text{TeV}$ [23, 24].

This paper is organized as follows: in section 2 the CMS detector is presented. Section 3 discusses the generation of monte carlo event simulation. Section 4 describes the calculation of acceptance values and reports the nominal value along with a comparison between acceptance at $\sqrt{s} = 5\,\text{TeV}$ and $\sqrt{s} = 13\,\text{TeV}$ . Systematic uncertainties on the acceptance values are described in section 5. The acceptance values and uncertainties for each signal process are summarized in section 6.

# Chapter 2

# CMS

The central feature of the CMS apparatus is a superconducting solenoid of 6 m internal diameter, providing a magnetic field of 3.8 T. Within the field volume are a silicon pixel and strip tracker, an electromagnetic calorimeter (ECAL) and a brass/scintillator hadron calorimeter (HCAL). Muons are detected in gas-ionization detectors embedded in the steel return yoke. In addition to the barrel and endcap detectors, CMS has extensive forward calorimetry.

CMS uses a right-handed coordinate system, with the origin at the nominal interaction point, the $x$-axis pointing to the center of the LHC ring, the $y$-axis pointing up (perpendicular to the LHC plane), and the $z$-axis along the anticlockwise-beam direction. The polar angle $\theta$ is measured from the positive $z$-axis and the azimuthal angle $\phi$ is measured in radians in the $xy$-plane. The pseudorapidity is given by $\eta = -\ln(\tan\theta/2)$.

The inner tracker measures charged particle trajectories in the pseudorapidity range $|\eta| < 2.5$. It consists of 1,440 silicon pixel and 15,148 silicon strip detector modules. It provides an impact parameter resolution of $\sim 15\,\mu\text{m}$ and a transverse momentum ($p_T$) resolution of about 1% for charged particles with $p_T \approx 40\,\text{GeV}$.

The electromagnetic calorimeter consists of nearly 76,000 lead tungstate crystals which provide coverage in pseudorapidity $|\eta| < 1.479$ in a cylindrical barrel region (EB) and $1.479 < |\eta| < 3.0$ in two endcap regions (EE). A preshower detector consisting of two planes of silicon sensors interleaved with a total of three radiation lengths of lead is located in front of the EE. The ECAL has an energy resolution of better than 0.5% for unconverted photons with transverse energies ($E_T$) above 100 GeV. The energy resolution is 3% or better for the range of electron energies relevant for this analysis. The hadronic barrel and endcap calorimeter are sampling devices with brass as the passive material and scintillator as active material. The combined calorimeter cells are grouped in projective towers of granularity $\Delta\eta \times \Delta\phi = 0.087 \times 0.087$ at central rapidities and $0.175 \times 0.175$ at forward rapidities.

Muons are detected in the pseudorapidity window $|\eta| < 2.4$, with detection planes based on three technologies: drift tubes, cathode strip chambers, and resistive plate chambers. A high-$p_T$ muon originating from the interaction point produces track segments in typically three or four muon stations. Matching these segments to tracks measured in the inner tracker results in a $p_T$ resolution between 1 and 2% for $p_T$ values up to 100 GeV.

The first level (L1) of the CMS trigger system, composed of custom hardware processors, is designed to select the most interesting events in less than 1 μs using information from the calorimeters and muon detectors. The High Level Trigger (HLT) processor farm further decreases the event rate to a few hundred hertz before data storage.

A more detailed description of CMS can be found elsewhere [5].

# Chapter 3

# Event Generation

One method to determine the kinematics of collision products is through simulation of particle collisions using Monte Carlo (MC) event generation. Monte Carlo event generators are widely used in particle physics for predictions in collider experiments and the design of new experiments.

Monte Carlo event generation has at its core the principle of Monte Carlo integration [25]. Since an integral can be written as the average over the integrand

$$I = \int_{x_1}^{x_2} \mathrm{d}x\, f(x) = (x_2 - x_1)\langle f(x)\rangle$$

then for N values of x chosen randomly from the range $(x_1, x_2)$ the average of $f(x)$ is a good estimate of $I$

$$I \approx \frac{1}{N}\sum_{i=1}^{N} W_i$$

where $W_i = (x_2 - x_1)f(x_i)$. The variance is given by

$$V_N = \frac{1}{N}\sum_{i=1}^{N} W_i^2 - \left[\frac{1}{N}\sum_{i=1}^{N} W_i\right]^2$$

giving uncertainty on the integral of $\sigma_{\mathrm{MC}} = \sqrt{\frac{V_N}{N}}$. The variance can be reduced by sampling overspecific non-uniform distributions of the phase space. Event generators apply this Monte Carlo integration to different steps along the particle interaction process, creating functional forms for probability amplitudes from the underlying physics principles.

Generators generally divide the process of simulating a proton-proton collision into the steps of a hard process, parton shower, hadronization, underlying event, and unstable particle decays [26]. The simulation begins by considering the process of interest and calculates the probability distribution of a momentum transfer process, the hard scattering, from perturbation theory using known Parton Distribution Functions (PDFs). PDFs give probability distributions for the momentum fraction carried by different flavors of partons within a proton colliding at some energy scale. QCD cannot predict the parton content of protons, so the PDFs are determined by fitting to experimental data of observables from various processes. There is no single universally accepted PDF, but rather a number of groups have created different PDF sets that differ in their choice of input data, the treatment of underlying perturbative QCD calculations, the treatment of heavy quarks, correlation with parameters such as the strong coupling constant $\alpha_s$, and the treatment of uncertainties [27]. Section 5.2 will further discuss uncertainty associated with the choice of PDF set.

Parton showering determines the behavior of the incoming and outgoing partons from a hard scattering process. From QCD it is known that color charges radiate gluons, which are themselves colored and lead to more radiaton. The showering of space with gluons is simulated by a sequential process that follows the scale of momentum transfer. Parton showering is an apporximation that works well in the collinear and soft limits. The collinear limit is the limit in which the openning angle $\theta$ between a quark and its radiated gluon goes to zero ($\theta \rightarrow 0, \pi$). The soft limit is the limit in which the energy fraction of the radiated gluon $z_g$ goes to zero ($z_g \rightarrow 0$). The parton showering description of final state radiation (FSR) is based in higher-order corrections to tree-level scattering diagrams and seeks to be fully inclusive in parton radiation. Initial state radiation (ISR) works backward from particular kinematic distribution of interacting partons to find the radiation that accompanies it. While the parton shower approximation is valid in collinear and soft limits, it does not describe the behavior within systems of hard, well-separated jets, best described by fixed-order matrix elements. Improvements are made by matching next-to-leading order (NLO) perturbative QCD calculations with a parton shower of jet internal structure.

Hadronization models include color confinement of parton groupings into color-neutral hadrons, which continue to decay as they propagate away from the ineraction point. During their propagation new hadrons are created, leading to the observed phenomenon of hadronic jets. The reconstruction of the hadronization process is important for understanding the origin of hadronic deposits.

Beside the hard scattering process of interest between particular partons of the colliding protons, the proton remnants interact with one another in the underlying event, giving off lots of soft hadrons that also decay.

In this analysis I compare two different Monte Carlo methods, Madgraph5_aMC@NLO and POWHEG, generators that are particularly well suited in combining NLO matrix elements with parton showers without double-counting [28, 29].

MadGraph5_aMC@NLO is a framework for studying Standard Model and Beyond Standard Model phenomenology through the computation of tree-level and next-to-leading order cross sections, their matching to parton shower simulations, and merging of various matrix-element multiplicities [28]. The core of the framework is the capability of computing tree-level and one-loop amplitudes for arbitrary processes, using the computations to predict physical observables. A variety of simulation possibilities are available in the single, process-independent framework, which allows the investigation of multiple possible scenarios and their guaranteed mutual consistency [30].

POWHEG is an alternative method for matching fixed-order computations to parton-shower event generators [29, 31].

Hadronization is performed using PYTHIA 8, a general-purpose event generator and the most-used generator for LHC physics [32, 33].

The production of Monte Carlo is performed by first making gridpacks of the desired processes, packages that contain information needed to run a physics process in an event generator on the CMS software framework CMSSW. The CMS software package GenProduction is a package for gridpack creation which contains a variety of generator tools, among them Powheg and Madgraph [34]. Gridpack production takes place on CERN's AFS batch network and on MIT's T3 Condor server [35, 36]. The generated gridpack is then used to make MC samples using specified configurations and run parameters by running in the CMSSW framework [37]. Finally the output Les Houches MC format is converted to the Bacon ntuple format for file storage, before being transformed to flat ntuples for analysis [38, 39].

# Chapter 4

# Acceptance

The acceptance of a decay channel is the ratio of events whose decay products have kinematics that fall within the kinematic acceptance region of the detector to the total number of events. The kinematic acceptance region of the detector is specified by the design and geometry of the detector.

The channels considered for this calculation are the leptonic decays of the Z boson, $Z \to l^+l^-$ and W boson, $W^\pm \to l^\pm\nu$, with $l^\pm = e^\pm, \mu^\pm$. The expected branching ratios in each leptonic channel are 11.1% for $W^\pm$ and 3.4% for $Z^0$.

The CMS fiducial region accepts electrons with pseudorapitity $\eta$ for values of $|\eta| < 1.44$ in the barrel or $1.57 < |\eta| < 2.5$ in the endcap and which have a transverse energy $E_T > 25\text{GeV}$. The fiducial region for muons requires $|\eta| < 2.4$ and $E_T > 25\text{GeV}$.

The acceptances calculated using both Madgraph and Powheg with PDF set NNPDF3.1 and Pythia for hadronization are given for electronic and muonic final states in tables 4.1 and 4.2 respectively.

The kinematic asymmetry observed between $W^+$ and $W^-$ bosons is due to the proton content of $u$ and $d$ quarks. Becasue $u$ quarks carry on average more proton momentum fraction than $d$ quarks, $W^+$ tends to be produced at larger rapidities, whereas $W^-$ is produced with a smaller rates and at central rapidities. This effect would not be observed in $p\bar{p}$ collisions, in which $W^+$ and $W^-$ are produced with equal rates [40].

To evaluate the differences in the kinematics as a function of the center-of-mass

| Process | Madgraph | Powheg |
|---|---|---|
| $W^+ \to e^+\nu$ | 0.541 | 0.538 |
| $W^- \to e^-\bar{\nu}$ | 0.505 | 0.505 |
| $W \to e\nu$ | 0.527 | 0.522 |
| $W^+ \to e^+\nu/W^- \to e^-\bar{\nu}$ | 1.070 | 1.065 |
| $Z \to ee$ | 0.418 | 0.418 |
| $W^+ \to e^+\nu/Z \to ee$ | 1.294 | 1.289 |
| $W^- \to e^-\bar{\nu}/Z \to ee$ | 1.209 | 1.210 |
| $W \to e\nu/Z \to ee$ | 1.260 | 1.250 |

Table 4.1: Acceptance from Madgraph and Powheg at 5 TeV for electronic final states

| Process | Madgraph | Powheg |
|---|---|---|
| $W^+ \to \mu^+\nu$ | 0.566 | 0.563 |
| $W^- \to \mu^-\bar{\nu}$ | 0.531 | 0.526 |
| $W \to \mu\nu$ | 0.552 | 0.545 |
| $W^+ \to \mu^+\nu/W^- \to \mu^-\bar{\nu}$ | 1.065 | 1.070 |
| $Z \to \mu\mu$ | 0.459 | 0.454 |
| $W^+ \to \mu^+\nu/Z \to \mu\mu$ | 1.232 | 1.240 |
| $W^- \to \mu^-\bar{\nu}/Z \to \mu\mu$ | 1.157 | 1.159 |
| $W \to \mu\nu/Z \to \mu\mu$ | 1.202 | 1.199 |

Table 4.2: Acceptance from Madgraph and Powheg at 5 TeV for muonic final states

energy, the ratio of the acceptances at $\sqrt{s} = 5\,\mathrm{TeV}$ and $\sqrt{s} = 13\,\mathrm{TeV}$ is calculated. The acceptace at 5 TeV is greater in the observable values considered except for the acceptance ratios of $W^- \to e^-\bar{\nu}/Z \to ee$ and $W^- \to \mu^-\bar{\nu}/Z \to \mu\mu$, indicating that the decrease in acceptance in the $W^-$ channel when going from 5 to 13 TeV is less than the decrease in acceptace in Z over the same range.

| Process | Madgraph | Powheg |
|---|---|---|
| $W^+ \to e^+\nu$ | 1.24 | 1.25 |
| $W^- \to e^-\bar{\nu}$ | 1.14 | 1.15 |
| $W \to e\nu$ | 1.20 | 1.20 |
| $W^+ \to e^+\nu/W^- \to e^-\bar{\nu}$ | 1.09 | 1.09 |
| $Z \to ee$ | 1.23 | 1.24 |
| $W^+ \to e^+\nu/Z \to ee$ | 1.01 | 1.01 |
| $W^- \to e^-\bar{\nu}/Z \to ee$ | 0.92 | 0.93 |
| $W \to e\nu/Z \to ee$ | 0.98 | 0.97 |

Table 4.3: Acceptance ratio 5 TeV/13 TeV from Madgraph and Powheg for electronic final states

| Process | Madgraph | Powheg |
|---|---|---|
| $W^+ \to \mu^+\nu$ | 1.26 | 1.26 |
| $W^- \to \mu^-\bar{\nu}$ | 1.15 | 1.15 |
| $W \to \mu\nu$ | 1.21 | 1.21 |
| $W^+ \to \mu^+\nu/W^- \to \mu^-\bar{\nu}$ | 1.10 | 1.09 |
| $Z \to \mu\mu$ | 1.25 | 1.24 |
| $W^+ \to \mu^+\nu/Z \to \mu\mu$ | 1.01 | 1.02 |
| $W^- \to \mu^-\bar{\nu}/Z \to \mu\mu$ | 0.92 | 0.93 |
| $W \to \mu\nu/Z \to \mu\mu$ | 0.98 | 0.97 |

Table 4.4: Acceptance ratio 5 TeV/13 TeV from Madgraph and Powheg for muonic final states

# Chapter 5

# Uncertainty

## 5.1 Statistical Uncertainty

The statistical uncertainty of the acceptance calculation is defined as

$$\sigma_a = \sqrt{\frac{a(1-a)}{N_{tot}}}$$

where $a$ is the acceptance and $N_{tot}$ is the total number of simulated events. With a sample size of one million events per decay channel, statistical uncertainty is limited to a per-mil level of the nominal acceptance value.

## 5.2 PDF + $\alpha_s$ Uncertainty

There is no single standard PDF for use in cross section calculations. Many different PDF sets have been made that differ in their choice of data sets, the treatment of unecertainties, and the form of parton parametrization [41]. The choice of PDF set can have a large impact on acceptance values, so it is necessary to quantify the uncertainty associated with the PDF set of choice.

The two main approaches to determining PDFs are using a Hessian covariance matrix, which minimizes a $\chi^2$ likelihood function, or through a Monte Carlo approach, minimizing $\chi^2$ for each of a sample of pseudo-data replicas [41].

The Monte Carlo approach is used by the NNPDF collaboration [42]. A large sample of pseudo-data replica sets is produced such that each replica has the same number of points as the input data. In the large replica limit, the central value of the $i$-th point is reproduced by the mean of its replica points, the experimental uncertainty is reproduced in the variance over replicas, and the correlation between data points is equal to the covariance over replicas [41].

NNPDF3.1 provides a method for measuring its uncertainty through replica PDF weights. For each event, there is a nominal value for the acceptance, and then a distribution of 100 PDF weights. Calculating the acceptance for each of the replica PDFs and evaluating their systematic uncertainties gives a distribution of acceptance values whose mean is the nominal acceptance value and standard deviation is the uncertainty associated with that PDF set.

Another component of parton distribution uncertainty comes from the value of $\alpha_s$, the strong coupling constant. The constant is one of the three fundamental coupling constants of the Standard Model, which vary as a function of the energy scale or momentum transfer Q of the particular process in question [43]. The strong coupling $\alpha_s(Q^2)$ decreases with increasing energy scale, leading to asymptotic freedom, a property of QCD that allows perturbative calculations of quarks interacting at high energies [44]. At the scale of Z boson mass $\alpha_s(M_Z^2)$ the determination of $\alpha_s$ has had a rich history of differing approaches that have resulted in values of being roughly between 0.117 and 0.125. The current world average $\alpha_s(M_Z^2) = 0.1185 \pm 0.0006$ [45].

The effect of uncertainty in the acceptance on the $\alpha_s$ value can be quantified by calculating acceptance using other $\alpha_s$ values and measuring the deviation from a nominal value. Another method, possible with the NNPDF approach, is combining $\alpha_s$ uncertainty with PDF uncertaninty by creating new PDF sets with all replica PDFs at different $\alpha_s$ values and calculating total uncertainty through replica PDF weights. These two methods are described by the PDF4LHC working group [41]. The advantage of the NNPDF data set is that determining the combined PDF + $\alpha_s$ uncertainty using the exact formula for central values removes the assumption of linear error propagation, which is necessary when calculating $\alpha_s$ and PDF uncertainty separately. The difference in the two methods, however, has been shown to be small [41]. This analysis will use summation in quadrature of the uncertainties because it is computationally simpler due to a summation over a smaller number of replica PDFs.

The combined PDF+$\alpha_s$ uncertainty is given in tables 5.1 and 5.2 for electrons and muons respectively.

| Process | Madgraph[%] | Powheg[%] |
|---|---|---|
| $W^+ \to e^+\nu$ | 0.2 | 0.3 |
| $W^- \to e^-\bar{\nu}$ | 0.3 | 0.4 |
| $W \to e\nu$ | 0.2 | 0.3 |
| $W^+ \to e^+\nu/W^- \to e^-\bar{\nu}$ | 0.3 | 0.4 |
| $Z \to ee$ | 0.4 | 0.4 |
| $W^+ \to e^+\nu/Z \to ee$ | 0.3 | 0.3 |
| $W^- \to e^-\bar{\nu}/Z \to ee$ | 0.4 | 0.3 |
| $W \to e\nu/Z \to ee$ | 0.3 | 0.2 |

Table 5.1: PDF + $\alpha_s$ uncertainty from Madgraph and Powheg at 5 TeV for electronic final states

| Process | Madgraph[%] | Powheg[%] |
|---|---|---|
| $W^+ \to \mu^+\nu$ | 0.3 | 0.2 |
| $W^- \to \mu^-\bar{\nu}$ | 0.4 | 0.4 |
| $W \to \mu\nu$ | 0.2 | 0.3 |
| $W^+ \to \mu^+\nu/W^- \to \mu^-\bar{\nu}$ | 0.4 | 0.4 |
| $Z \to \mu\mu$ | 0.4 | 0.4 |
| $W^+ \to \mu^+\nu/Z \to \mu\mu$ | 0.3 | 0.3 |
| $W^- \to \mu^-\bar{\nu}/Z \to \mu\mu$ | 0.4 | 0.3 |
| $W \to \mu\nu/Z \to \mu\mu$ | 0.3 | 0.3 |

Table 5.2: PDF + $\alpha_s$ uncertainty from Madgraph and Powheg at 5 TeV for muonic final states

## 5.3 Factorization and Renormalization

QCD calculation to fixed order is dependent on factorization ($\mu_F$) and renormalization ($\mu_R$) scales. A widely-used method to calculate uncertainty associated with higher-order perturbation is to vary the scale factors about a central value defined by the physical scale of the computation [45]. For a central value $Q$, a typical range of variation is $Q/2 < \mu_R, \mu_F < 2Q$, with an additional constraint that $\frac{1}{2} < \frac{\mu_F}{\mu_R} < 2$. This method is the one adopted by the NNPDF working group, and is used to calculate higher-order uncertainties on NLO processes [42].

For this analysis the uncertainty from scale variations is taken to be the envelope of acceptance values from each of the seven scale variations, performed on the central PDF of NNPDF3.1.

The scale uncertainties are given in tables 5.3 and 5.4 for electrons and muons respectively.

| Process | Madgraph[%] | Powheg[%] |
|---|---|---|
| $W^+ \to e^+\nu$ | 0.08 | 0.11 |
| $W^- \to e^-\bar{\nu}$ | 0.05 | 0.15 |
| $W \to e\nu$ | 0.04 | 0.13 |
| $W^+ \to e^+\nu/W^- \to e^-\bar{\nu}$ | 0.13 | 0.04 |
| $Z \to ee$ | 0.31 | 0.05 |
| $W^+ \to e^+\nu/Z \to ee$ | 0.37 | 0.08 |
| $W^- \to e^-\bar{\nu}/Z \to ee$ | 0.31 | 0.10 |
| $W \to e\nu/Z \to ee$ | 0.33 | 0.08 |

Table 5.3: Scale uncertainty from Madgraph and Powheg at 5 TeV for electronic final states

| Process | Madgraph[%] | Powheg[%] |
|---|---|---|
| $W^+ \to \mu^+\nu$ | 0.05 | 0.10 |
| $W^- \to \mu^-\bar{\nu}$ | 0.02 | 0.15 |
| $W \to \mu\nu$ | 0.03 | 0.13 |
| $W^+ \to \mu^+\nu/W^- \to \mu^-\bar{\nu}$ | 0.06 | 0.05 |
| $Z \to \mu\mu$ | 0.13 | 0.05 |
| $W^+ \to \mu^+\nu/Z \to \mu\mu$ | 0.15 | 0.07 |
| $W^- \to \mu^-\bar{\nu}/Z \to \mu\mu$ | 0.13 | 0.10 |
| $W \to \mu\nu/Z \to \mu\mu$ | 0.14 | 0.08 |

Table 5.4: Scale uncertainty from Madgraph and Powheg at 5TeV for muonic final states

# Chapter 6

# Summary

The acceptances for lepotnic decays of Z and W bosons in proton-proton collisions at a center of mass energy of $\sqrt{s} = 5\,\text{TeV}$ and their associated uncertainties have been calculated, and are summarized in tables 6.1 and 6.2 for Madgraph and Powheg generators respectively. The theoretical uncertainty of PDF + $\alpha_s$ values forms the dominant contribution to the uncertainty. The acceptance is one part of the analysis necessary to compute the inclusive cross section of W and Z boson production at $\sqrt{s} = 5\,\text{TeV}$ using LHC data from 2015 and 2017. From the formula $\sigma_{tot} \times B = \frac{N}{A \times \epsilon \times \mathcal{L}}$ the other quantities that must be measured are the detector efficiency $\epsilon$, the luminosity $\mathcal{L}$, and the number of signal events $N$ corresponding to particular decay processes. The measurement of the cross section will be a valuable validation of the Standard Model and will be useful in further constraining Parton Distribution Functions.

| Process | Acceptance | Stat. [%] | PDF+$\alpha_s$ [%] | >NLO [%] | Total [%] |
|---|---|---|---|---|---|
| $W^+ \to e^+\nu$ | 0.541 | 0.1 | 0.2 | 0.1 | 0.2 |
| $W^- \to e^-\bar{\nu}$ | 0.505 | 0.1 | 0.3 | 0.0 | 0.4 |
| $W \to e\nu$ | 0.527 | 0.1 | 0.2 | 0.0 | 0.2 |
| $W^+ \to e^+\nu/W^- \to e^-\bar{\nu}$ | 1.070 | 0.1 | 0.3 | 0.1 | 0.4 |
| $Z \to ee$ | 0.418 | 0.1 | 0.4 | 0.3 | 0.5 |
| $W^+ \to e^+\nu/Z \to ee$ | 1.294 | 0.1 | 0.3 | 0.4 | 0.5 |
| $W^- \to e^-\bar{\nu}/Z \to ee$ | 1.209 | 0.1 | 0.4 | 0.3 | 0.5 |
| $W \to e\nu/Z \to ee$ | 1.260 | 0.1 | 0.3 | 0.3 | 0.5 |
| $W^+ \to \mu^+\nu$ | 0.566 | 0.1 | 0.3 | 0.1 | 0.3 |
| $W^- \to \mu^-\bar{\nu}$ | 0.531 | 0.1 | 0.4 | 0.0 | 0.4 |
| $W \to \mu\nu$ | 0.552 | 0.1 | 0.2 | 0.0 | 0.2 |
| $W^+ \to \mu^+\nu/W^- \to \mu^-\bar{\nu}$ | 1.065 | 0.1 | 0.4 | 0.1 | 0.4 |
| $Z \to \mu\mu$ | 0.459 | 0.1 | 0.4 | 0.1 | 0.4 |
| $W^+ \to \mu^+\nu/Z \to \mu\mu$ | 1.232 | 0.1 | 0.3 | 0.2 | 0.4 |
| $W^- \to \mu^-\bar{\nu}/Z \to \mu\mu$ | 1.157 | 0.1 | 0.4 | 0.1 | 0.5 |
| $W \to \mu\nu/Z \to \mu\mu$ | 1.202 | 0.1 | 0.3 | 0.1 | 0.4 |

Table 6.1: Summary of acceptance and uncertainties from Madgraph at 5 TeV.

| Process | Acceptance | Stat. [%] | PDF+$\alpha_s$ [%] | >NLO [%] | Total [%] |
|---|---|---|---|---|---|
| $W^+ \to e^+\nu$ | 0.538 | 0.1 | 0.3 | 0.1 | 0.3 |
| $W^- \to e^-\bar{\nu}$ | 0.505 | 0.1 | 0.4 | 0.1 | 0.4 |
| $W \to e\nu$ | 0.522 | 0.1 | 0.3 | 0.1 | 0.3 |
| $W^+ \to e^+\nu/W^- \to e^-\bar{\nu}$ | 1.065 | 0.1 | 0.4 | 0.0 | 0.4 |
| $Z \to ee$ | 0.418 | 0.1 | 0.4 | 0.1 | 0.4 |
| $W^+ \to e^+\nu/Z \to ee$ | 1.289 | 0.1 | 0.3 | 0.1 | 0.3 |
| $W^- \to e^-\bar{\nu}/Z \to ee$ | 1.210 | 0.1 | 0.3 | 0.1 | 0.3 |
| $W \to e\nu/Z \to ee$ | 1.250 | 0.1 | 0.2 | 0.1 | 0.3 |
| $W^+ \to \mu^+\nu$ | 0.563 | 0.1 | 0.2 | 0.1 | 0.3 |
| $W^- \to \mu^-\bar{\nu}$ | 0.526 | 0.1 | 0.4 | 0.2 | 0.4 |
| $W \to \mu\nu$ | 0.545 | 0.1 | 0.3 | 0.1 | 0.3 |
| $W^+ \to \mu^+\nu/W^- \to \mu^-\bar{\nu}$ | 1.070 | 0.1 | 0.4 | 0.1 | 0.4 |
| $Z \to \mu\mu$ | 0.454 | 0.1 | 0.4 | 0.1 | 0.4 |
| $W^+ \to \mu^+\nu/Z \to \mu\mu$ | 1.240 | 0.1 | 0.3 | 0.1 | 0.3 |
| $W^- \to \mu^-\bar{\nu}/Z \to \mu\mu$ | 1.159 | 0.1 | 0.3 | 0.1 | 0.3 |
| $W \to \mu\nu/Z \to \mu\mu$ | 1.199 | 0.1 | 0.3 | 0.1 | 0.3 |

Table 6.2: Summary of acceptance and uncertainties from Powheg at 5 TeV.

# Bibliography


[1] K. Dilsiz and E. Tiras, "Cross Section Predictions of W ($W \to \ell^{\pm}\nu$) and Z ($Z \to \ell^{+}\ell^{-}$) Bosons in Association with Jets in pp Collisions," 2017.

[2] O. Brüning, *Large Hadron Collider Design Report*, vol. 1. European Organization for Nuclear Research, 2004.

[3] P. H. Garbincius, "Tevatron collider operations and plans," in *Proceedings, 39th Rencontres de Moriond, 04 Electroweak interactions and unified theories: La Thuile, Aosta, Italy, Mar 21-28, 2004*, pp. 19–26, 2004.

[4] T. Csörgö *et al.*, "Elastic Scattering and Total Cross-Section in $p + p$ reactions measured by the LHC Experiment TOTEM at $\sqrt{s} = 7$ TeV," *Prog. Theor. Phys. Suppl.*, vol. 193, pp. 180–183, 2012.

[5] T. C. Collaboration, "The cms experiment at the cern lhc," *Journal of Instrumentation*, vol. 3, no. 08, p. S08004.

[6] G. Aad, E. Abat, J. Abdallah, A. Abdelalim, A. Abdesselam, O. Abdinov, B. Abi, M. Abolins, H. Abramowicz, E. Acerbi, *et al.*, "The atlas experiment at the cern large hadron collider," *Journal of Instrumentation*, vol. 3, no. 8, pp. S08003–S08003, 2008.

[7] T. Han and B. Zhang, "Signatures for majorana neutrinos at hadron colliders," *Phys. Rev. Lett.*, vol. 97, p. 171804, Oct 2006.

[8] F. Hasert, S. Kabe, W. Krenz, J. Von Krogh, D. Lanske, J. Morfin, K. Schultze, H. Weerts, G. Bertrand-Coremans, J. Sacton, *et al.*, "Observation of neutrino-like interactions without muon or electron in the gargamelle neutrino experiment," *Nuclear Physics B*, vol. 73, no. 1, pp. 1–22, 1974.

[9] F. Hasert, H. Faissner, W. Krenz, J. Von Krogh, D. Lanske, J. Morfin, K. Schultze, H. Weerts, G. Bertrand-Coremans, J. Lemonne, *et al.*, "Search for elastic muon-neutrino electron scattering," *Physics letters B*, vol. 46, no. 1, pp. 121–124, 1973.

[10] "Ua1," *CERN Document Server*, Jan 2013.

[11] "Ua2," *CERN Document Server*, Jan 2013.

[12] M. Banner, R. Battiston, P. Bloch, F. Bonaudi, K. Borer, M. Borghini, J.-C. Chollet, A. Clark, C. Conta, P. Darriulat, *et al.*, "Observation of single isolated electrons of high transverse momentum in events with missing transverse energy at the cern pp collider," *Physics Letters B*, vol. 122, no. 5-6, pp. 476–485, 1983.

[13] G. T. Arnison, G. Jorat, D. Smith, J. Rich, W. Scott, A. Astbury, F. Lacava, D. Holthuizen, R. Frühwirth, R. Kinnunen, *et al.*, "Experimental observation of isolated large transverse energy electrons with associated missing energy at $\sqrt{s} = 540$ gev," *phys. Lett. B*, vol. 122, no. CERN-EP-83-13, pp. 103–116, 1983.

[14] P. Bagnaia *et al.*, "Evidence for Z0 —> e+ e- at the CERN anti-p p Collider," *Phys. Lett.*, vol. 129B, pp. 130–140, 1983.

[15] "The nobel prize in physics 1984," *Nobelprize.org*, 2014.

[16] "The large electron-positron collider," *CERN Document Server*, Jul 2012.

[17] R. A$\beta$mann, M. Lamont, S. Myers, *et al.*, "A brief history of the lep collider," *Nuclear Physics B-Proceedings Supplements*, vol. 109, no. 2-3, pp. 17–31, 2002.

[18] W. de Boer, "Precision Experiments at LEP," *Adv. Ser. Direct. High Energy Phys.*, vol. 23, pp. 107–136, 2015.

[19] "Cms luminosity calibration for the pp reference run at $\sqrt{s} = 5.02$ TeV," Tech. Rep. CMS-PAS-LUM-16-001, CERN, Geneva, 2016.

[20] C. Collaboration, "Measurements of Inclusive $W$ and $Z$ Cross Sections in $pp$ Collisions at $\sqrt{s} = 7$ TeV," *JHEP*, vol. 01, p. 080, 2011.

[21] C. Collaboration, "Measurement of the Inclusive $W$ and $Z$ Production Cross Sections in $pp$ Collisions at $\sqrt{s} = 7$ TeV," *JHEP*, vol. 10, p. 132, 2011.

[22] C. Collaboration, "Measurement of inclusive W and Z boson production cross sections in pp collisions at $\sqrt{s} = 8$ TeV," *Phys. Rev. Lett.*, vol. 112, p. 191802, 2014.

[23] A. Collaboration, "Measurement of $W^{\pm}$ and $Z$-boson production cross sections in $pp$ collisions at $\sqrt{s} = 13$ TeV with the ATLAS detector," *Phys. Lett.*, vol. B759, pp. 601–621, 2016.

[24] C. Collaboration, "Measurement of inclusive W and Z boson production cross sections in pp collisions at sqrt(s)=13 TeV," 2015.

[25] A. Papaefstathiou, "How-to: Write a parton-level Monte Carlo event generator," 2014.

[26] M. H. Seymour and M. Marx, "Monte Carlo Event Generators," in *Proceedings, 69th Scottish Universities Summer School in Physics : LHC Phenomenology (SUSSP69): St.Andrews, Scotland, August 19-September 1, 2012*, pp. 287–319, 2013.

[27] R. Placakyte, "Parton Distribution Functions," in *Proceedings, 31st International Conference on Physics in collisions (PIC 2011): Vancouver, Canada, August 28-September 1, 2011*, 2011.

[28] J. Alwall, R. Frederix, S. Frixione, V. Hirschi, F. Maltoni, O. Mattelaer, H. S. Shao, T. Stelzer, P. Torrielli, and M. Zaro, "The automated computation of tree-level and next-to-leading order differential cross sections, and their matching to parton shower simulations," *JHEP*, vol. 07, p. 079, 2014.

[29] P. Nason, "A New method for combining NLO QCD with shower Monte Carlo algorithms," *JHEP*, vol. 11, p. 040, 2004.

[30] S. Frixione and B. R. Webber, "Matching NLO QCD computations and parton shower simulations," *JHEP*, vol. 06, p. 029, 2002.

[31] S. Alioli, P. Nason, C. Oleari, and E. Re, "NLO vector-boson production matched with shower in POWHEG," *JHEP*, vol. 07, p. 060, 2008.

[32] T. Sjostrand, S. Mrenna, and P. Z. Skands, "A Brief Introduction to PYTHIA 8.1," *Comput. Phys. Commun.*, vol. 178, pp. 852–867, 2008.

[33] A. Buckley *et al.*, "General-purpose event generators for LHC physics," *Phys. Rept.*, vol. 504, pp. 145–233, 2011.

[34] CMS-SW, "Genproductions," *GitHub repository*, 2018.

[35] A. Kupich, "Batch jobs on lxplus," *CERN Twiki*, 2016.

[36] MIT-HEP, "Cmsaf userguide," *CMSAF Twiki*, 2010.

[37] C. Collaboration, "Cmssw application framework," *CERN Twiki*, 2017.

[38] MIT-HEP, "Baconana," *GitHub repository*, 2016.

[39] MIT-HEP, "Baconprod," *GitHub repository*, 2016.

[40] S. Catani, G. Ferrera, and M. Grazzini, "W Boson Production at Hadron Colliders: The Lepton Charge Asymmetry in NNLO QCD," *JHEP*, vol. 05, p. 006, 2010.

[41] S. Alekhin *et al.*, "The PDF4LHC Working Group Interim Report," 2011.

[42] R. D. Ball *et al.*, "Parton distributions from high-precision collider data," *Eur. Phys. J.*, vol. C77, no. 10, p. 663, 2017.

[43] G. Dissertori, "The Determination of the Strong Coupling Constant," *Adv. Ser. Direct. High Energy Phys.*, vol. 26, pp. 113–128, 2016.

[44] D. J. Gross, "The discovery of asymptotic freedom and the emergence of qcd," *Proceedings of the National Academy of Sciences of the United States of America*, vol. 102, no. 26, pp. 9099–9108, 2005.

[45] S. Bethke, G. Dissertori, and G. Salam, *Quantum Chromodynamics*, vol. 38 of *090001*. Chin Phyis C, 9 ed., 2014.